Table of contents

Supplementary Figure S1

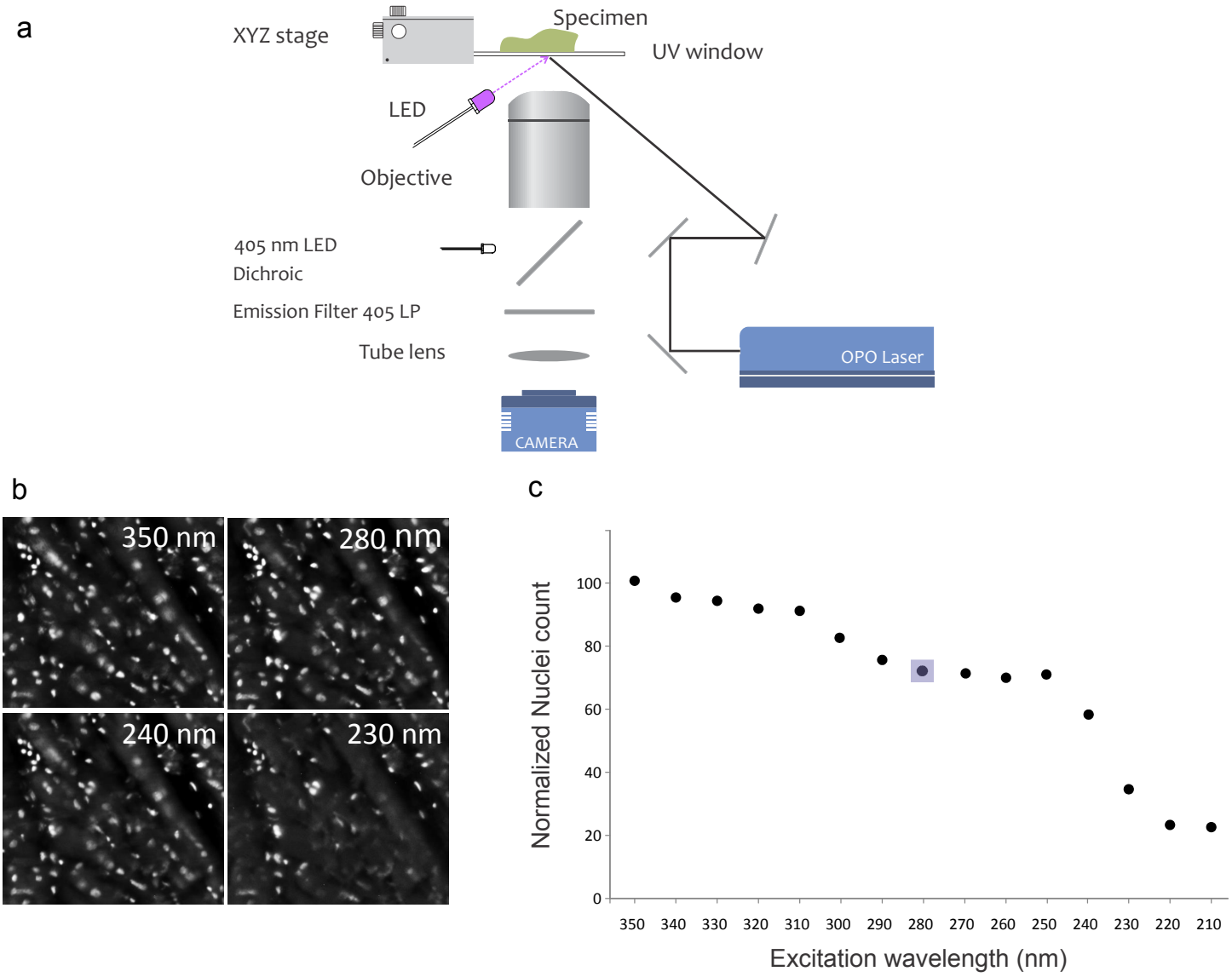

Figure S1: Analysis of MUSE wavelength-depth sensitivity.

a, Schematic of system used for depth-dependence experiment. In addition to the MUSE 280-nm UV LED, light from a tunable laser was directed to the sample at the same incidence angle. **b**, Fresh porcine cardiac tissue was stained overnight with Hoechst 33342 (to label nuclei) and then imaged at different excitation wavelengths using an OPO tunable laser as the light source (between 350 to 210 nm in 10-nm steps). At each wavelength, a series of images was taken while focusing from the surface to ~40 microns below. Maximum projection representations are presented for 4 selected wavelengths. Representative images are shown, indicating that more nuclei were visible deeper at longer excitation wavelengths. **c**, Nuclei were enumerated manually on each maximum projection image, and the number of visible nuclei (normalized to a maximum value of 100) was plotted as a function of excitation wavelength.

Supplementary Figure S2

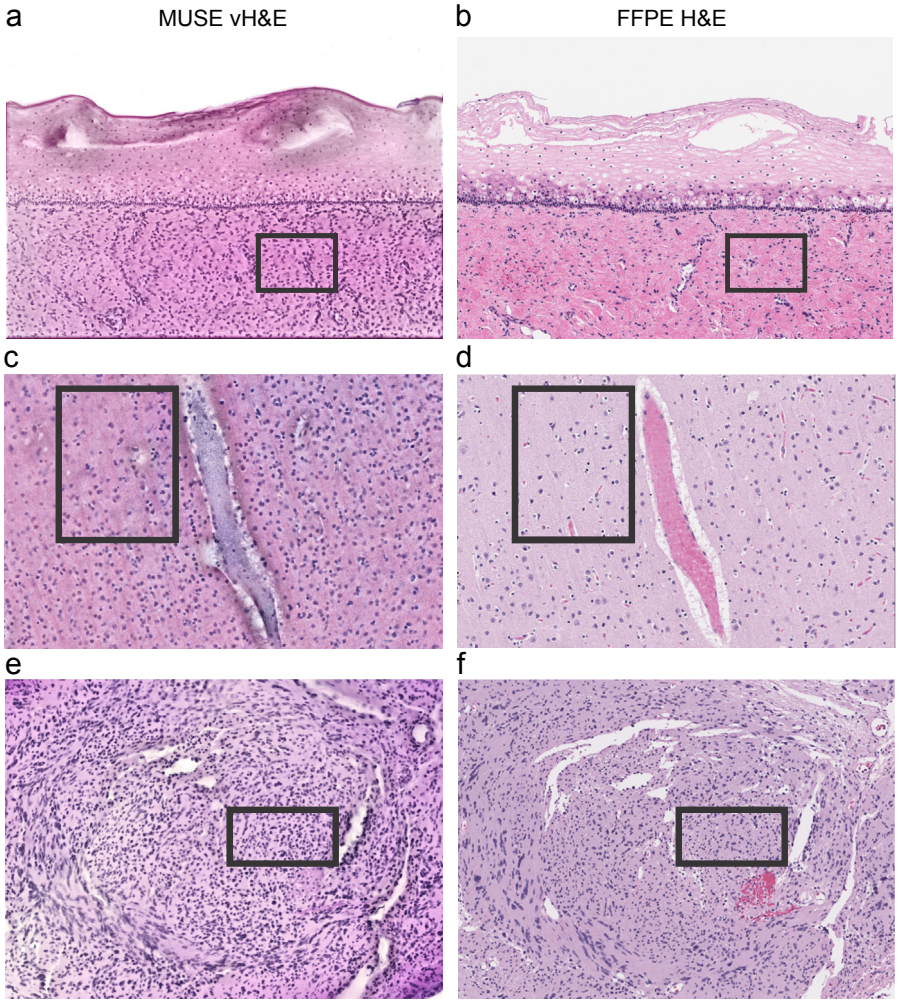

	Nuclei in H&E	Nuclei in MUSE	% difference
Cervix	95	153	61
Visual Cortex	80	122	52
Schwannoma	232	279	20

Figure S2: Comparison of effective imaging depth, MUSE (left column) vs. FFPE 5-μm sections (right column).

MUSE images were obtained from deparaffinized tissue after blocks were sectioned and H&E-stained slides were prepared. MUSE imaging was performed with rhodamine and Hoechst staining and the resulting images were color-mapped to vH&E. Equivalent regions are shown for both methods. Nuclei were manually counted in the boxes shown, and results given in the table. **a, b**, cervix; **c, d,** brain, visual cortex; **e, f**, cranial nerve schwannoma. Approximately 20 to 60% more nuclei are visible in the MUSE images compared to their conventional FFPE H&E equivalents. Accordingly, it may be necessary to adjust estimates of the cellularity expected for different tissues and disease processes with MUSE.

Supplementary Figure S3

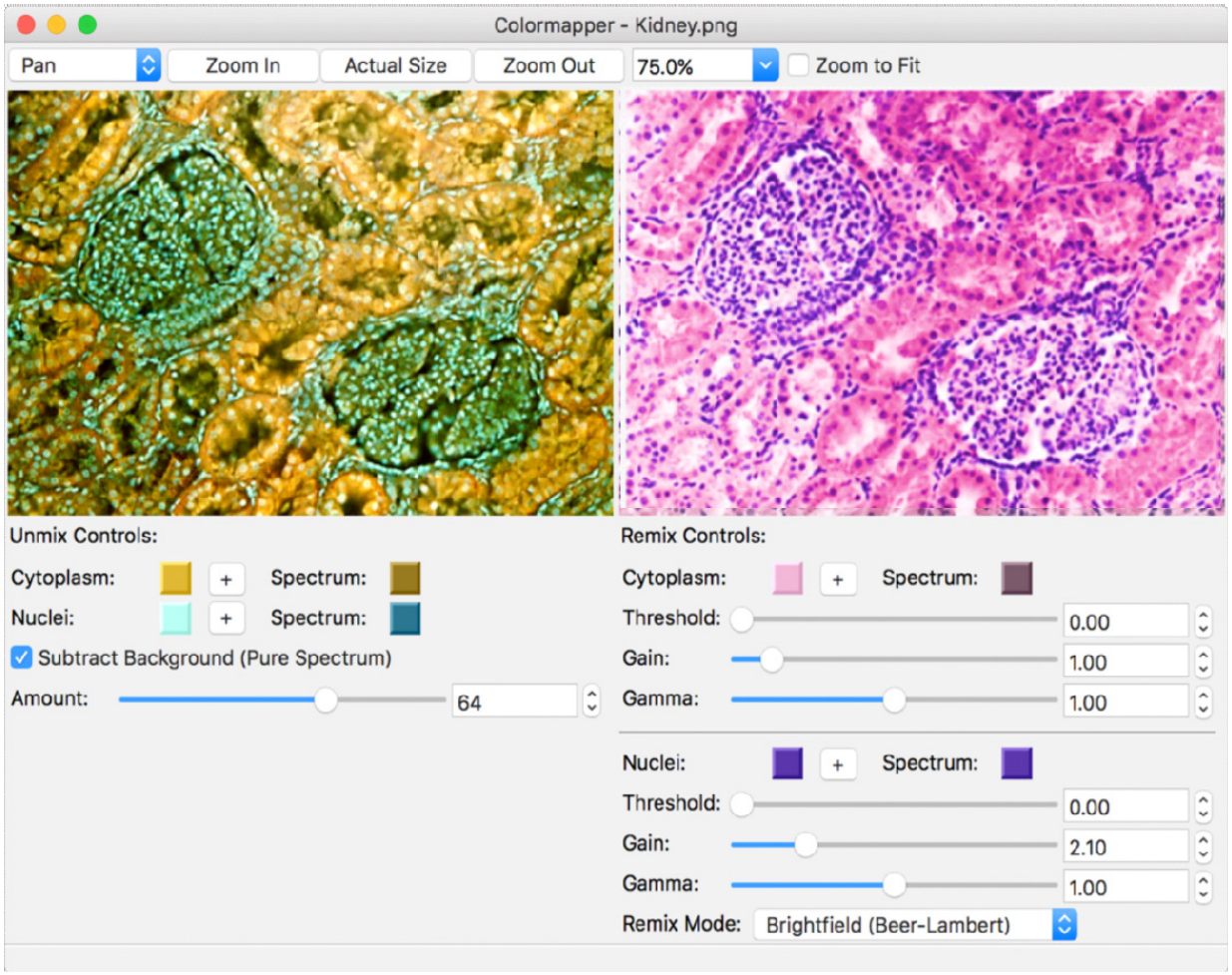

Figure S3: The graphical interface to the color remapping method.
The user can control unmixing by selecting nuclear and non-nuclear RGB spectra by clicking on specific locations, and correcting for the presence of spectrally mixed signals. The unmixed channels are then colorized in user-selectable hues and recombined with a variety of mixing techniques (Beer-Lambert is shown), with the interface allowing independent adjustment of offset, brightness, and gamma of each component. This approach allows for customization of the color-mapping to suit user preference and the tinctorial properties of the stains employed, and can be applied automatically and in real-time during imaging.

Supplementary Figure S4

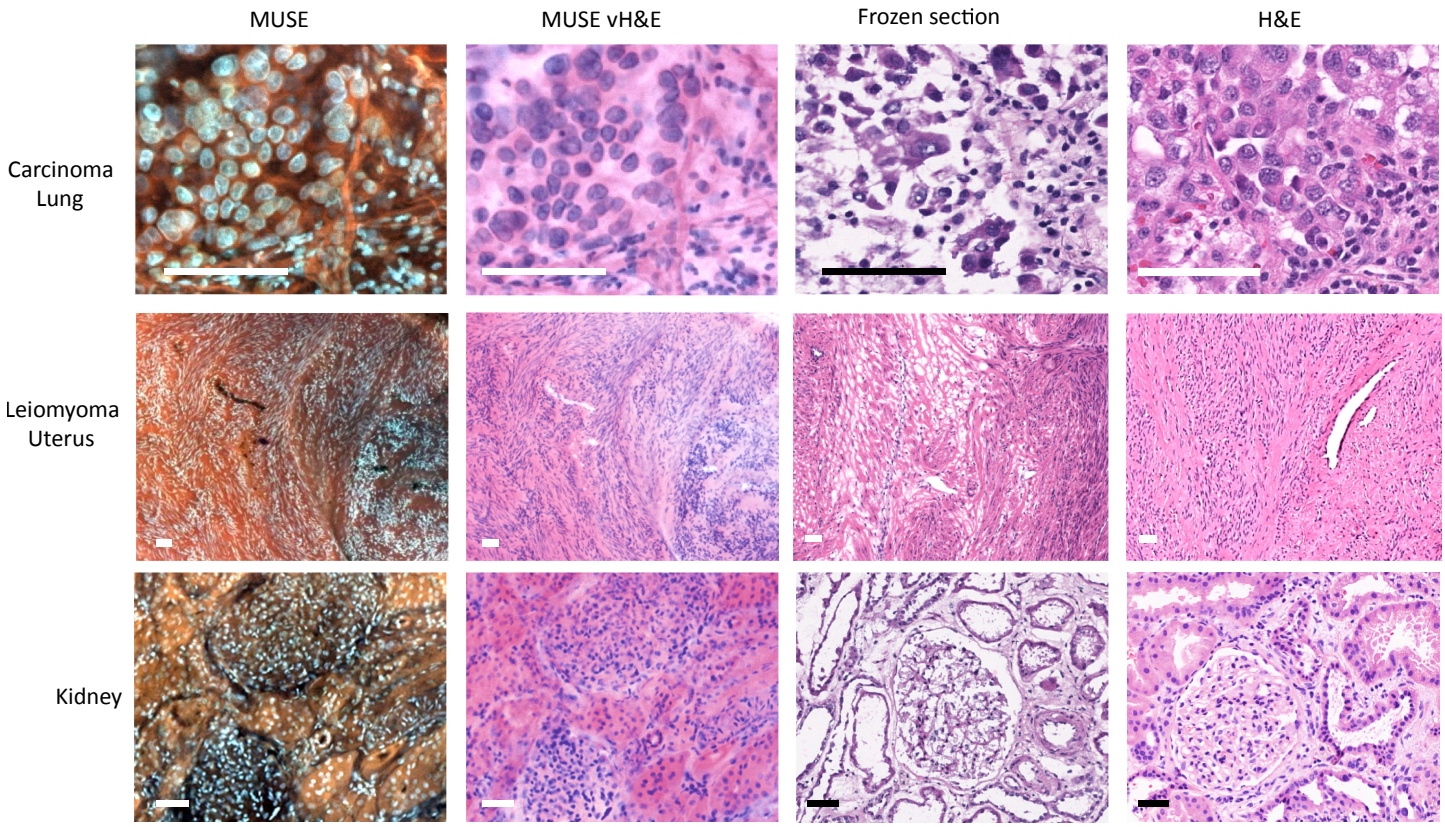

Figure S4: Fresh tissues (lung, uterus, kidney) imaged using MUSE, and compared to frozen sections and FFPE histology from the same specimens.

Left two columns, MUSE and color-mapped vH&E versions of the same image. Right two columns, H&E-stained frozen section and conventional FFPE histology from the corresponding specimen. The MUSE and MUSE vH&E images are morphologcially similar to their FFPE counterpart, while significant freezing artifacts are visible in the frozen sections. Scale bar = 20μm for the top row, 100μm for the middle and bottoms rows.

Supplementary Figure S5

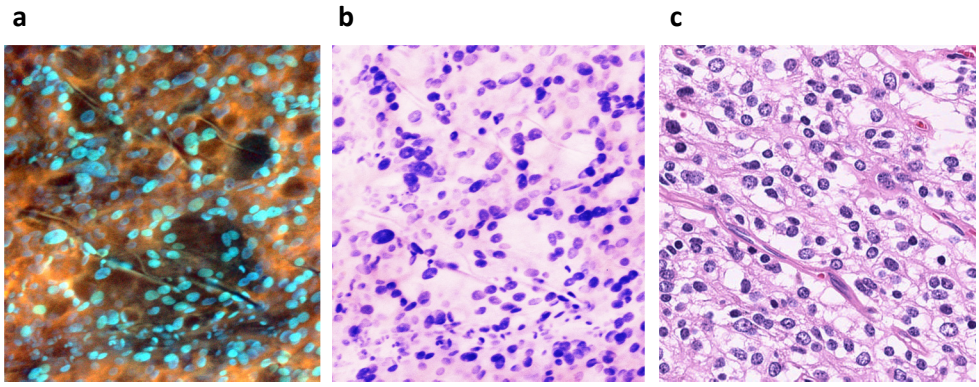

Tumor Type	*Technique*	Path. # 1		Path. # 2		Path. # 3		Path. # 4		*Combined Accuracy (%)*
		Correct	Wrong	Correct	Wrong	Correct	Wrong	Correct	Wrong	
Di? use Astrocytic Oligodendroglial	MUSE	6	1	7	0	6	1	7	0	93
	H&E	6	1	7	0	7	0	7	0	96
Meningioma	MUSE	8	0	8	0	8	0	8	0	100
	H&E	8	0	8	0	8	0	8	0	100
Ependymal and Choroid Plexus	MUSE	2	1	3	0	3	0	3	0	92
	H&E	3	0	3	0	3	0	2	1	92
Cranial or Paraspinal Nerves	MUSE	3	0	3	0	3	0	3	0	100
	H&E	3	0	3	0	3	0	3	0	100
Metastatic	MUSE	3	0	3	0	3	0	3	0	100
	H&E	3	0	3	0	3	0	3	0	100
Combined	*Accuracy (%)*	94		100		98		98		97

Path. = Pathologist

Figure S5: Preliminary validation of MUSE for CNS lesion identification.

24 CNS lesions represented by 3-4 images each, comprising the diagnostic categories shown in the lower panel, were imaged via MUSE and the resulting fluorescence and vH&E images were shown to a panel of 4 pathologists (not neuropathology specialists) who were unaware of the clinical diagnoses. Top panel: **a**, Original MUSE image; **b**, corresponding vH&E, and **c**, paired FFPE H&E images from an oligodendroglioma. Correlation of their diagnoses with ground-truth obtained from paired H&E slides as determined by a board-certified neuropathologist is indicated. It is notable that accuracy was excellent when either fluorescence or vH&E images were presented, indicating that it may not always be necessary to convert the native images to pseudo-brightfield in every instance. Scale bar = 100 μm.

Supplementary Figure S6

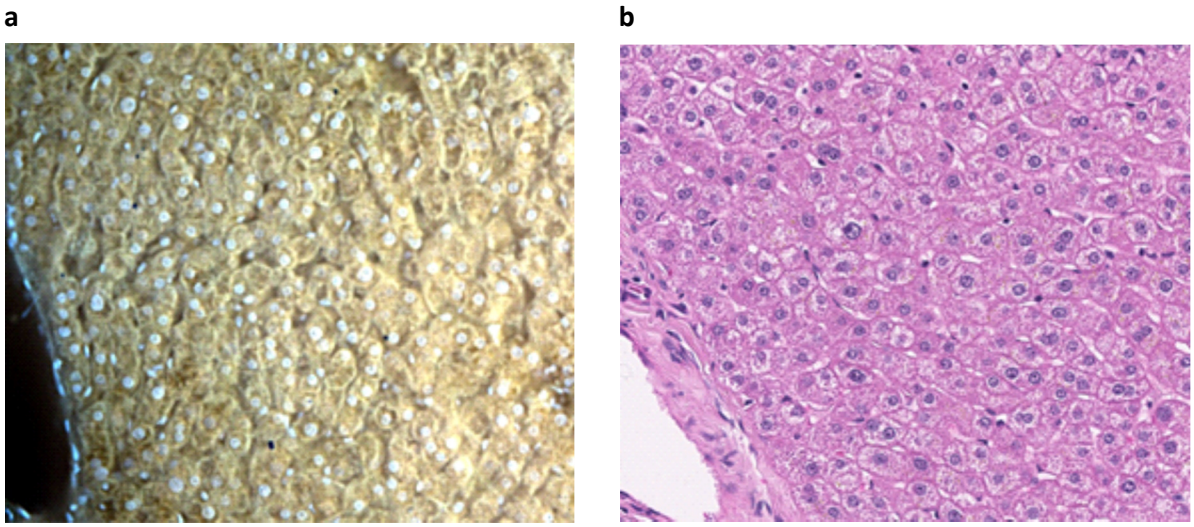

Figure S6. Prior MUSE imaging does not adversely affect subsequent FFPE processing and H&E staining. An example is shown of a formalin-fixed liver stained with rhodamine, and Hoechst imaged via MUSE (a). It was subsequently paraffin-embedded, sectioned, stained with H&E and imaged on an Aperio whole slide scanner (b); similar regions from each imaging method are shown. No deterioration of H&E image quality was evident.

Supplementary Figure S7

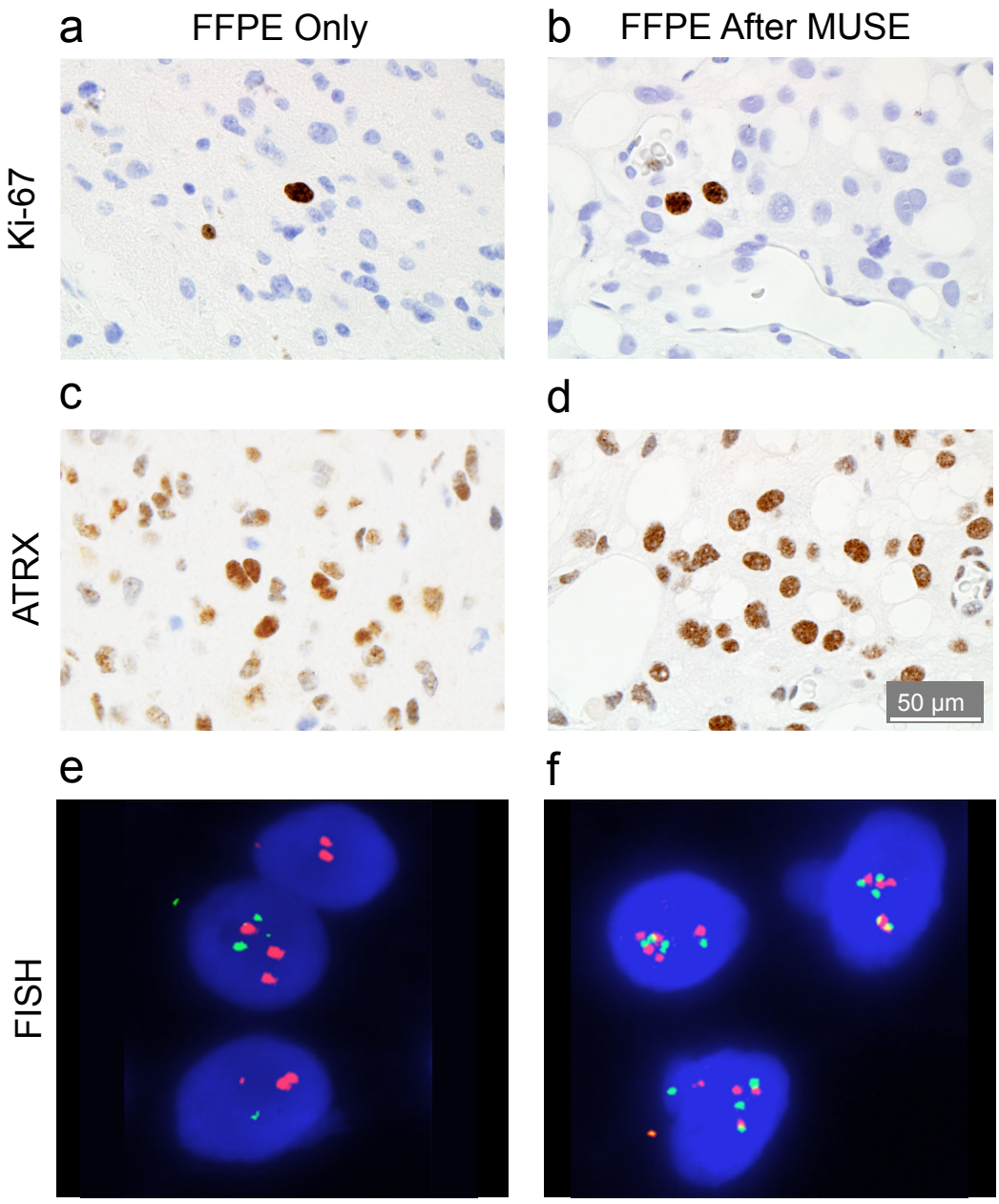

Figure S7: Lack of effect of MUSE processing on subsequent IHC and FISH testing.

A formalin-fixed resection specimen from an oligodendroglioma was split into two portions. One was immediately processed for immunohistochemistry (IHC) and fluorescence in-situ hybridization (FISH) (left column) and the other was submitted for IHC and FISH after staining with rhodamine and Hoechst and MUSE (right column). **a, b,** IHC staining for Ki-67; **c,d,** IHC staining for ATRX; **e,f** FISH staining for 1p19q alteration in interphase cells. No technical differences were noted in IHC or FISH testing between samples that were or were not exposed to prior MUSE staining and imaging.

Supplementary Figure S8

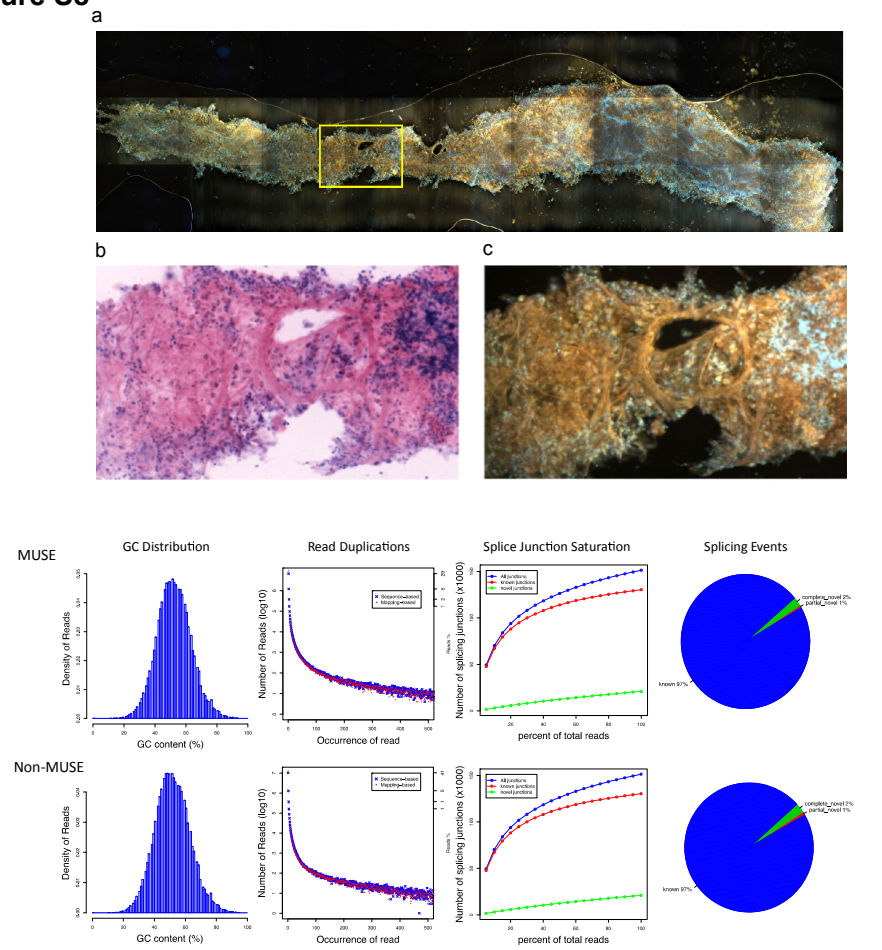

Metric	MUSE sample	%	non-MUSE sample	%
Total reads	27376784	100	29669036	100
Reads with mate sequenced	27376784	100	29669036	100
Reads without mate sequenced	0	0	0	0
QC-failed reads	0	0	0	0
Mapped reads	26617265	97.2	28864772	97.3
Unmapped reads	759519	2.8	804264	2.7
Singleton reads (itself mapped; mate unmapped)	236379	0.9	272258	0.9
Paired reads (itself & mate mapped)	26380886	96.4	28592514	96.4
Properly paired reads	25254632	92.2	27257196	91.9
Not properly paired reads (discordant)	1126254	4.1	1335318	4.5
Reads with MAPQ [40:inf)	21429756	78.3	23853096	80.4

Figure S8: Assessing quality of RNA extracted from MUSE-imaged core needle-extracted tissue.

In order determine whether MUSE imaging would impair the quality of subsequently extracted RNA, core needle specimens were removed from an excised lung tumor. One core, similar to **a**, was stained with rhodamine and Hoechst for 10 s and imaged over a number of 10X fields (total imaging time about 2 min); the other core was kept moist in PBS before both were snap-frozen in liquid N_2 and processed for RNA-Seq. RIN scores for MUSE and non-MUSE samples were 7.9 and 8.4 respectively. **b**, Graphical depiction of a number of quantitative comparisons between the two specimens following RNA-Seq analysis—no appreciable differences were evident. **c**, Additional numerical metrics comparing MUSE- and non-MUSE-processed samples also demonstrated no systemic differences, indicating MUSE imaging may prove to be compatible with downstream molecular profiling.

Supplementary Figure S9

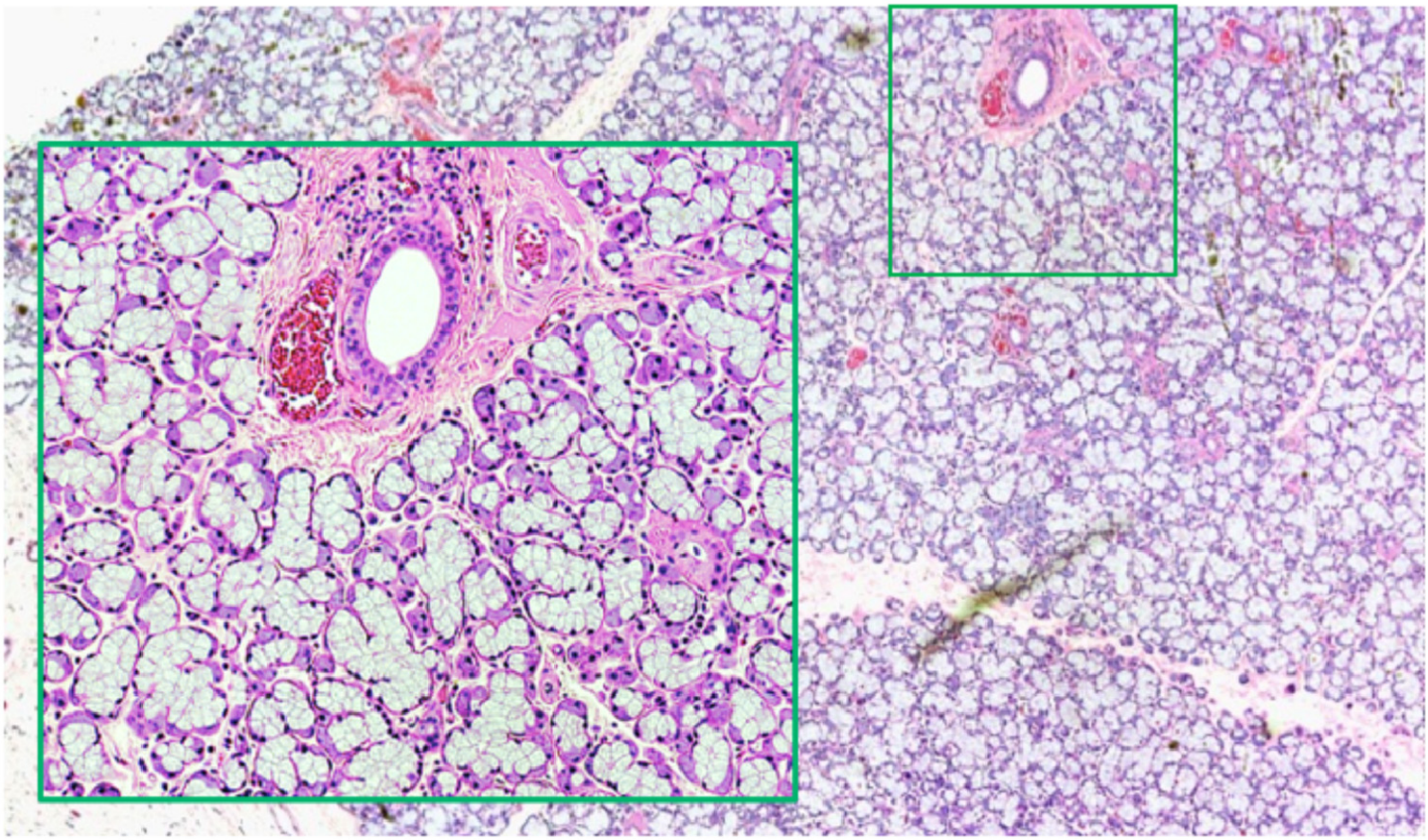

Supplemental Figure S9: Suitability of MUSE instruments for standard brightfield whole-slide imaging.

By using a slide-holder in place of the sapphire sample support, and suitable white-light illumination, which can be as simple as overhead room lighting, whole-slide images from conventionally prepared and H&E-stained whole slides can be obtained. Depending on the optics, the resolution may not equal that of a dedicated whole-slide scanner, but it can be a convenience to rapidly acquire a reasonable slide image.

Supplementary Figure S10

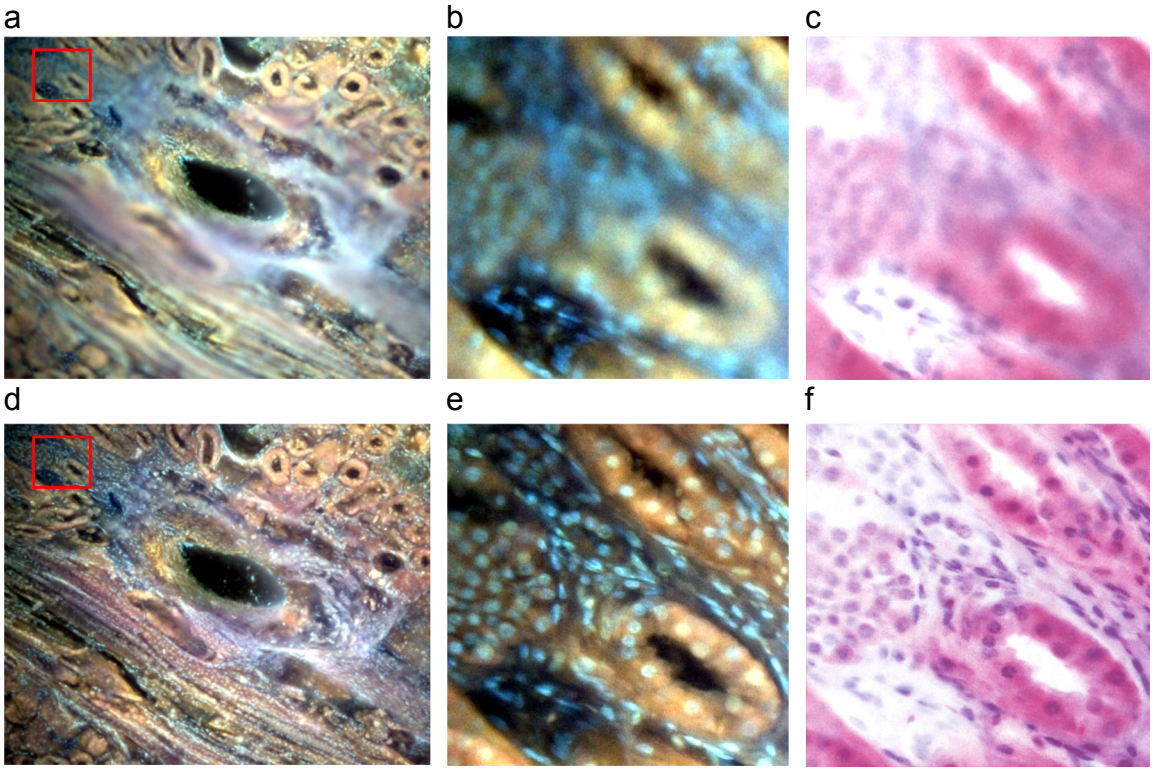

Figure S10: Extended depth-of-field.

a, A single image of kidney with an uneven cut surface, taken at a best axial lens position for overall focus. Considerable out-of-focus regions above and below the focal plane are visible. **b**, Zoomed-in region (red rectangle in left column). **c,** Color-mapped H&E version of the same region. **d**, Multiple images at different Z-positions were acquired and an extended depth-of-field image was computed using an ImageJ plugin as described in Supplementary Note 4. **e, f,** Zoomed-in regions before and after color mapping (compare **b** and **e**). Scale bar = 100μm

Supplementary Note 1. Imaging depth as a function of excitation wavelength
Figure S1 demonstrates that the density of nuclei visible on maximum projection (which is directly related to the laser penetration depth) decreases monotonically as the excitation was tuned from 350 to 210 nm. However, while the number of countable nuclei decreased modestly between 350 nm and 310 nm and remained more or less constant from 280 nm to 250 nm, steeper declines are observed in the 310-280-nm- and in the 250-230-nm-spectral ranges. For wavelength shorter than 230 nm, only the most superficial nuclei were visible. Based on additional criteria that included dye absorption/excitation spectra and the cost and power of different ranges of sub-300-nm LEDs, sources with peak emission around 280 nm appeared most practical, and were used for all subsequent experiments. When similar regions of the same tissues are imaged via MUSE and conventional histology, nuclear counting indicated approximately 20% to 60% greater effective section thickness with MUSE (Fig. S2).

Supplementary Note 2. Deep-UV excitation of standard fluorescent dyes.
One of the key features of MUSE that it takes advantage of the property of UV light to excite conventional fluorescent dyes and cause them to emit in their familiar visible range; such staining behavior is required to provide image contrast for diagnosis. As illustrated in Fig. 1d, most common organic dyes exhibit a small Stokes' shift, that is, having excitation ranges located spectrally near to their emitted light. However, many dyes also share a common excitation regime in the sub-300-nm range, permitting the convenient staining and imaging of tissues exposed to a variety of dyes, solely and in combination. We investigated the use of a variety of fluorescent dyes for which, after excitation from the ground state (S0) to the second excited state (S2) the transition decay to S0 competes with vibrational relaxation to S1, which is a more probable decay path [1]. The nonradiative relaxation of the dye molecules to the S1-excited state is then followed by radiative S1- to-S0 relaxation, leading to photon emission in the dyes' familiar, typically visible-range, spectrum.

Supplementary Note 3. Conversion from MUSE fluorescence to virtual H&E
Pathologists are trained to diagnose disease using microscopic examination of H&E-stained tissue slides, and rely on the familiar shades of pink and purple to facilitate visual recognition of different structures and diseases. The unfamiliar hues emitted by the fluorescent dyes and captured by MUSE will require viewers to become acclimatized—a process that appears to happen rapidly as H&E and MUSE images of similar tissues are compared. To address this issue, MUSE images can be converted into ones that mimic H&E-stained brightfield histology though color-mapping image processing algorithms.

There are several methods for converting fluorescent images to mimic brightfield H&E slides. The method proposed by Gareau [2] assumes that there are separate grayscale fluorescent measurements of the nuclear and cytoplasm stains, often captured using optical filters to isolate each stain. These images are then combined by inverting and colorizing the individual signals, then subtracting the results from a pure white background. This approach has been successfully applied to images captured by a variety of fluorescence-based microscopes, including nonlinear microscopy (NLM) [3] and dual-channel confocal microscopy [4]. Other approaches similar to the one described here utilize the Beer-Lambert absorption law to weight recombination intensities [5]. By using this relevant physical model, along with non-negatively constrained unmixing, realistic imitators of H&E appearance can be achieved. Images captured with an RGB color camera were typically used to create virtual H&E-like results, applying unmixing procedures similar to those previously described [5] for estimation of abundances of multiplexed targets [6] or to remove endogenous autofluorescence [7]. What differentiates our method is that we isolate the contributions of the nuclear and cytoplasm stains using broadband RGB data.

The user can select the RGB values (as a 3-channel spectrum) of the representative nuclear and non-nuclear tissue elements directly from the image prior to unmixing. In the example shown, as Hoechst stains principally nuclei whereas rhodamine stains most tissue elements including nuclei, it can be important to characterize a pure Hoechst "spectrum"—that does not also include contributions from rhodamine—prior to performing

unmixing [8]. The resulting unmixed image then combines nuclear staining attributable to both dyes. This technique allows the images to resemble more closely those from conventional H&E-stained slides, because it reflects the fact that in conventional H&E-stained slides, both, eosin and hematoxylin stain the nuclei.

The algorithmic underpinnings for the Beer-Lambert color-mapping process are given below. We let $Y(x, y, \lambda)$ denote the observed fluorescent intensity in the λ-color channel at pixel (x, y). This intensity is modeled as the superposition of a small number, k, of fluorescent components having emission spectra denoted by $\alpha_i(\lambda)$, i = 1,…,k, which can be written as

$$Y(x,y,\lambda) = \sum_{i=1}^{k} \alpha_i(\lambda) X_i(x,y) + W(x,y,\lambda)$$

where $X_i(x,y)$ is the abundance of component i at pixel (x, y), and $W(x, y, \lambda)$ is a term that captures both the system noise and modeling error. The components $X_i(x,y)$, i = 1,…,k can be found through nonnegative least-squares (NNLS). The required optimization problem is highly parallelizable, as we can independently solve for the solution at every pixel. OpenCL, a parallel computing framework for writing high-performance code for use on GPUs, was used to speed up unmixing. A gradient projection algorithm, written in C, was used to solve the optimization. This algorithm is also known as a projected Landweber method [9]. Once estimates of the relative abundances of each component are known, a Beer-Lambert physical model is used to generate the converted image. The absorption spectra are denoted $\beta_i(\lambda)$ of each component (hematoxylin and eosin) to produce a recolored image $Z(x, y, \lambda)$ via

$$Z(x,y,\lambda) = \exp\left(-\sum_{i=1}^{k} \beta_i(\lambda) X_i(x,y)\right).$$

Note that image intensities are assumed to fall in the range [0, 1], and the resulting image would need to be scaled by 255, then be converted to an 8-bit integer (for example) for storage as a digital image. In practice, it is often desirable to adjust the individual contrast and relative concentrations of the fluorescent abundances used to mimic the hematoxylin and eosin concentrations in the computed brightfield image.

Supplementary Note 4. Extended depth of field

It is important that the images be in best possible focus. The samples are more challenging than conventional thin sections on mounted on glass slides, as they are usually cut by hand, and must be gently compressed against a flat optical surface. Beyond this, the fact that the samples do have real surface topography means that some parts will be out of focus when using high-NA lenses with small depth of focus (DOF). It's possible to increase the DOF by taking a number of images at different Z-positions, and merging the results using point-spread-function-based techniques, as shown in Fig. S8 [10]. This can be accomplished using a standard Z-stage or a mechanically re-focused lens. The image is reconstructed using the ImageJ plugin downloadable from http://bigwww.epfl.ch/demo/edf/. In addition, this plug-in also allows for 3D (depth-resolved) reconstruction of the surface profile.

Supplementary Table 1 MUSE vs. H&E Surgical Pathology Validation Study

			H&E Diagnosis—Pathologist 1		MUSE Diagnosis—Pathologist 2
	Tissue		Fresh/Fixed	H&E comments	
1	ovary	Fr	corpus luteum/ luteoma		benign ovary with corpus lutea
2	colon	Fr	normal colon		normal colon
3	breast	Fr	benign breast		benign breast (atrophic)
4	prostate	Fr	glandular hyperplasia		benign prostate
5	prostate	Fr	glandular hyperplasia		benign prostate
6	lung	Fr	adenocarcinoma	favor lepidic predominant type, non-mucinous	adenocarcinoma
7	prostate	Fr	adenocarcinoma, Gleason pattern 4+3		adenocarcinoma, Gleason pattern 4+3
8	retro-peritoneal mass	Fr	sarcoma, high grade	DDX includes leiomyosarcoma, rhabdomyosarcoma, and undifferentiated pleomorphic NOS	poorly differentiated malignant neoplasm, favor rhabdomyosarcoma
9	thyroid	Fx	papillary thyroid carcinoma	tall-cell variant features	carcinoma, papillary with tall cell features
10	lung	Fx	adenocarcinoma, NOS		NSCLC favor adenocarcinoma
11	colon	Fx	adenocarcinoma, NOS		carcinoma with invasion into muscularis
12	colon	Fx	adenocarcinoma, NOS		adenoma with carcinoma in situ (invasion not demonstrated in images presented)
13	liver	Fx	adenocarcinoma, NOS		carcinoma, favor metastatic
14	kidney	Fx	renal cell carcinoma, clear cell type,	nuclear grade 2	renal cell carcinoma, partially cystic.
15	breast	Fx	invasive mammary carcinoma, no special type (ductal)	Grade 2?	invasive mammary carcinoma

16	ovary	Fx	malignant tumor		papillary serous borderline
17	"gyn"	Fx	myometrial smooth muscle		leiomyoma
18	skin	Fx	benign skin,	consistent with a plantar or palmar surface	hyperkeratosis with chronic perivascular and interface dermatitis
19	lung	Fx	adenocarcinoma,	well differentiated lepidic predominant type	adenocarcinoma, lepidic predominant
20	bowel	Fx	well differentiated neuroendocrine tumor (carcinoid)		carcinoid (would also r/o GIST)
21	thyroid	Fx	benign thyroid tissue	could be part of a multinodular hyperplasia; minimal changes suggesting palpation thyroiditis	follicular nodules with chronic thyroiditis
22[a]	ovary	Fx	granulosa cell tumor		carcinoma, high grade (met v. primary)
23	ovary	Fx	mucinous cystadenoma		mucinous cystadenoma (possible borderline)
24[b]	Vulva	Fx	adenocarcinoma, NOS		carcinoma, squamous cell invasive
25	ovary	Fx	serous borderline tumor	could be serous carcinoma; can't tell from just three fields	papillary serous at least borderline, favor carcinoma
26	thyroid	Fx	papillary thyroid carcinoma	mix of follicular and papillary architectures	papillary carcinoma, conventional
27	kidney	Fx	renal cell carcinoma, clear cell type,	nuclear grade 2	renal cell carcinoma
28[c]	lung	Fx	non-small cell carcinoma of lung		carcinoma, favor neuroendocrine
29	ovary	Fx	serous borderline tumor	could be serous carcinoma; can't tell from just two fields	papillary serous neoplasm, favor borderline (invasion not demonstrated)
30	kidney	Fx	renal cell carcinoma, clear cell type,	nuclear grade 3	renal carcinoma favor papillary
31	breast	Fx	benign atrophic breast		Breast benign lobule
32	breast	Fx	ductal carcinoma in-situ	no clear cut invasion in these images	DCIS cribriform low grade

33	colon	Fx	adenocarcinoma, NOS		carcinoma, invasive into lamina propria.
34	kidney	Fx	renal cell carcinoma, clear cell type,	nuclear grade 2	renal cell carcinoma, clear cell
35	skin	Fx	benign skin,	consistent with back	benign skin
36	thyroid	Fx	poorly differentiated thyroid carcinoma		thyroid carcinoma favor insular variant
37	kidney	Fx	renal cell carcinoma, clear cell type,	nuclear grade 2	renal cell carcinoma, clear cell
38	"gyn"	Fx	endometrioid carcinoma	FIGO grade 1, arising in EIN	carcinoma, favor endometrioid
39	ovary	Fx	low grade serous tumor, at least borderline		carcinoma
40	adrenal	Fx	pheochromocytoma	histology does not predict malignant behavior in this tumor	involved by neoplasm, favor pheochromocytoma
41	adrenal	Fx	adrenal cortical adenoma or carcinoma	histology alone is not sufficient to distinguish adenoma v carcinoma of this type.	adrenal neoplasm, including pheo, adenoma, carcinoma (IHC required)
2	appendix	Fx	appendiceal carcinoid (low grade neuroendocrine tumor)	suspect high grade neuroendocrine tumor based on necrosis but images do not show mitotic activity	Favor carcinoid (IHC required)

Notes.

a. Both reviewers indicated the presence of a neoplasm. However, granulosa tumor was the H&E diagnosis, and the MUSE reviewer, after reviewing the case histology, concluded that the correct diagnosis could have been made from the MUSE images. In particular, nuclear grooving was evident, but had not been appreciated initially.

b. Distinction between adenocarcinoma and squamous carcinoma can be difficult and may require IHC.

c. H&E diagnosis was non-small cell lung carcinoma. The MUSE reviewer indicated carcinoma, but suggested neuroendocrine.

Supplementary References

1 Ashutosh, S. & Stephen, G. (John Wiley & Sons, Inc., New York, 1999).

2 Gareau, D. S. Feasibility of digitally stained multimodal confocal mosaics to simulate histopathology. *J. Biomed. Opt.* **14**, 034050--034050-034055, doi:10.1117/1.3149853 (2009).

3 Tao, Y. K. *et al.* Assessment of breast pathologies using nonlinear microscopy. *Proc. Natl. Acad. Sci.* **111**, 15304--15309, doi:10.1073/pnas.1416955111 (2014).

4 Elfer, K., Sholl, A., Miller, C. & Brown, J. Q. Vol. 9537 95370K--95370K-95373 (2015).

5 Kenny, K. B. (US Patent US 8,639,013 B2, 2011).

6 Keshava, N. & Mustard, J. F. Spectral unmixing. *IEEE Signal. Proc. Mag.* **19**, 44--57, doi:10.1109/79.974727 (2002).

7 Ghaznavi, F., Evans, A., Madabhushi, A. & Feldman, M. Digital imaging in pathology: Whole-slide imaging and beyond. *Annu. Rev. Pathol.: Mech. Dis.* **8**, 331--359, doi:10.1146/annurev-pathol-011811-120902 (2013).

8 Taylor, C. R. & Levenson, R. M. Quantification of immunohistochemistry---issues concerning methods, utility and semiquantitative assessment II. *Histopathol.* **49**, 411--424, doi:10.1111/j.1365-2559.2006.02513.x (2006).

9 Johansson, B. *et al.* The application of an oblique-projected Landweber method to a model of supervised learning. *Math. Comput. Model.* **43**, 892--909, doi:http://dx.doi.org/10.1016/j.mcm.2005.12.010 (2006).

10 Aguet, F., Van De Ville, D. & Unser, M. Model-based 2.5-d deconvolution for extended depth of field in brightfield microscopy. *IEEE Trans Image Process* **17**, 1144-1153, doi:10.1109/TIP.2008.924393 (2008).